

Provided for non-commercial research and education use.  
Not for reproduction, distribution or commercial use.



This article appeared in a journal published by Elsevier. The attached copy is furnished to the author for internal non-commercial research and education use, including for instruction at the authors institution and sharing with colleagues.

Other uses, including reproduction and distribution, or selling or licensing copies, or posting to personal, institutional or third party websites are prohibited.

In most cases authors are permitted to post their version of the article (e.g. in Word or Tex form) to their personal website or institutional repository. Authors requiring further information regarding Elsevier's archiving and manuscript policies are encouraged to visit:

<http://www.elsevier.com/copyright>



Contents lists available at ScienceDirect

## Computers in Biology and Medicine

journal homepage: [www.elsevier.com/locate/cbm](http://www.elsevier.com/locate/cbm)

## Detection of type II endoleaks in abdominal aortic aneurysms after endovascular repair

I. Macía<sup>a,b</sup>, M. Graña<sup>b,\*</sup>, J. Maiora<sup>b</sup>, C. Paloc<sup>a</sup>, Mariano de Blas<sup>c</sup>

<sup>a</sup> Vicomtech, Visual Communications Technologies Centre, Spain

<sup>b</sup> Grupo de Inteligencia Computacional, UPV/EHU, Spain

<sup>c</sup> Interventional Radiology Service, Donostia Hospital, Donostia-San Sebastián, Spain

### ARTICLE INFO

#### Article history:

Received 23 July 2010

Accepted 22 July 2011

#### Keywords:

Abdominal aortic aneurysm  
Endovascular aneurysm repair  
Endoleak detection  
Thrombus segmentation  
Neural networks  
Image processing

### ABSTRACT

Abdominal aortic aneurysm (AAA) is a condition where the weakening of the aortic wall leads to its widening and the generation of a thrombus. To prevent a possible rupture of the aortic wall, AAA can be treated non-invasively by means of the endovascular aneurysm repair technique (EVAR), consisting of placing a stent-graft inside the aorta by a catheter to exclude the aneurysm sac from the blood circulation. A major complication is the presence of liquid blood turbulences, called endoleaks, in the thrombus formed in the space between the aortic wall and the stent-graft. In this paper we propose an automatic method for the detection of type II endoleaks in computer tomography angiography (CTA) images. The lumen and thrombus in the aneurysm area are first segmented using a radial model approach. Then, these regions are split into Thrombus Connected Components (TCCs) using a watershed-based segmentation and geometric and image content-based characteristics are obtained for each TCC. Finally, TCCs are classified into endoleaks and non-endoleaks using a multilayer Perceptron (MLP) trained on manual labeled sample TCCs provided by experts.

© 2011 Elsevier Ltd. All rights reserved.

### 1. Introduction

Abdominal aortic aneurysm (AAA) is a cardiovascular disease that is caused by a degenerative process of the aortic wall, which leads to its wear and deformation. If not treated, AAAs increase in size progressively and may result in rupture, and, eventually, death [15]. There are currently two main repair techniques for AAAs: open aneurysm repair (OR) and endovascular aneurysm repair (EVAR). EVAR is a minimally invasive technique consisting in placing an endograft, typically a cloth graft with a stent exoskeleton, within the lumen of the AAA, extending distally into the iliac arteries. This serves as a bypass and decreases the pressure exerted on the aortic wall, leading to a reduction in AAA size over time and a decrease in the risk of aortic rupture. An intraluminal thrombus (ILT) forms in the majority of abdominal aortic aneurysms. Correctly excluded aneurysms progressively shrink after EVAR surgery. Nevertheless, there may be leaks into or from the sac due to incorrect positioning, displacement or torsion of the graft, that is, liquid blood may appear inside the thrombus after EVAR. This effect is called an *endoleak*.

In this paper, we address two computational problems directed to the semi-automatic detection of endoleaks in CTA images.

First the AAA thrombus segmentation procedure which is done on a radial representation of the thrombus contours, enhanced with *a priori* knowledge and modeling of spatial coherence. This segmentation is needed in order to localize the endoleaks inside the thrombus image area. Second we propose a multilayer perceptron (MLP) [7] classifier for the automatic detection of (type II) endoleaks applied on the segmented lumen and thrombus of the AAA.

The detection of endoleaks is performed classifying thrombus connected components (TCCs) obtained from segmentation of the thrombus image area using a morphological grayscale watershed transform [3]. Classification features are geometric and image content-based characteristics of the TCCs. Ground truth for training the MLP are provided by the human experts that classify a large sample of TCCs into two classes “endoleak” and “no-endoleak”.

Experimental results over a collection of AAA scans provided by the show good performance that the MLP is able to characterize and correctly classify image regions inside the aneurysm corresponding to endoleaks after training over the provided labeled sample. Endoleaks appear seldom in the image data from treated AAA patients. Therefore, it is extremely difficult to find data for the validation of the proposed approach. For this reason our system has to be validated at the level of 2D slices, however a 3D extension is easy and will be done when more data is available for training and validation.

The contents of the paper are as follows: Section 2 gives the review the current approaches dealing with the problem of

\* Corresponding author.

URLS: <http://www.vicomtech.org> (I. Macía), <http://www.ehu.es/ccwintoc> (M. Graña).

thrombus segmentation and endoleak detection. Section 3 describes the thrombus segmentation and image processing methods and the design of the MLP for endoleak detection. Section 4 presents the experimental data and the results obtained with the proposed processing sequence. Finally, Section 4.1 gives some summary conclusions and directions for further work.

## 2. State of the art review

Close follow-up is required after endovascular repair, with CTA scans performed at one, six, and 12 months, and with a year periodicity after that. In order to assess the evolution of the aortic wall aneurysm sac, the aneurysm must be delineated in the images. The aorta lumen usually presents a high contrast in CTA, however, segmentation of the aneurysm thrombus is not a trivial task, due to low-contrast in the ILT region compared to adjacent structures (see Fig. 1). Manual segmentation by trained radiologists is a time-consuming task, and suffers from intra- and inter-observer variability. With the advent of last generation CT scanners, the number of slices per examination has increased, and the manual delineation of tenths to hundreds of slices becomes impossible on a clinical routine. Hence, the development of automatic or semi-automatic methods for the segmentation of AAAs is required. Furthermore, quantitative assessment of evolution of aneurysms after EVAR is usually performed by taking the largest diameter or cross-sectional area on a single slice, but volume measurement has been demonstrated to show the smallest intra-observer variability [16]. Thus, a (semi)automatic segmentation method would allow patient follow-up using volumetric measurements of aneurysm size.

A major risk of EVAR interventions is the presence of liquid blood inside the aneurysm sac, called *endoleak*. Although endoleaks are more likely to occur soon after the intervention, lifelong surveillance is required [9]. Endoleaks can be classified into several types, depending on the cause [18,19]. The most common are type II endoleaks, which arise from persistent retrograde flow in collateral vessel branches. Some type II endoleak thrombose spontaneously but some others don't, causing an increase in aneurysm size and risk of rupture. In these cases intervention is required, usually consisting in an embolization of collateral branches.

The characteristic CTA image feature of an endoleak is the presence of brighter material inside the excluded aneurysm sac [12,14] (see Fig. 1 right). Type II endoleaks typically appear in the periphery of the aneurysm sac without touching the stent [12]. The actual image intensity value of the endoleak varies and depends on the size of the leak and the distribution of contrast material at the moment the image was acquired. They can be confused with calcifications which appear in the outer aortic wall and are brighter, whereas type II endoleaks appear typically close to the wall perfusing into the sac and showing an amorphous shape (see Fig. 1). Since these endoleaks can be approximately characterized, we believe that an automatic detection and quantification system for type II

endoleaks are possible and would be very helpful, specially in cases where endoleaks are not very clearly visible but may be made evident from the analysis of subtle changes in the image content.

Thrombus segmentation of AAAs has been addressed in the literature using several approaches [13,5,11,21,2,10]. The works presented in [13,5] need initial manual delineations to initialize their models; the method by de Bruijne et al. [5] needs posterior user intervention in case of thrombus boundary overflow. Olabarriaga et al. [11] employ a binary thresholding to obtain the lumen, which is used as an initialization for a deformable model to segment the thrombus. Simple thresholding takes into account other tissues not connected to the lumen, so further processing is usually needed to avoid those structures. Furthermore, the use of deformable models needs fine parameter tuning to obtain acceptable results. In this regard, Subasic et al. [13] use a level-set approach, de Bruijne et al. [5] apply an active shape model (ASM). Zhuge et al. [21] also present an algorithm based on a *level-set* approach whose main advantage is the automatization and parameter insensitivity. Nevertheless, the required computing time (in the order of several minutes) is a main drawback. The work by Borghi et al. [2] makes use of region growing segmentation techniques in order to obtain the lumen boundary, but then use manual delineation of the aneurysm wall to obtain a 3D model of thoracic aortic aneurysm (TAA). A computational study of the drag forces that can produce stent displacement is given in [6] for TAA. The work of Lee et al. [10] performs an initial estimation of the lumen region by region growing after anisotropic smoothing. Then both the lumen and the thrombotic surfaces are built up using a 3D graph search with cost functions specially designed for the lumen and the thrombus surfaces. Parameter values are empirically set, and the algorithm requires interactive guidance of the thrombus segmentation. Regarding endoleak detection, we have not found any work in the literature that addresses the problem of automatic detection and quantification of endoleaks in CTA images.

## 3. Methods

An overview of the processes involved in the automatic endoleak classification system can be seen in Fig. 2. First the aneurysm lumen and thrombus are segmented using the proposed segmentation method described in Section 3.1. We start from a segmentation of the lumen, based on a 3D region growing algorithm, followed by the calculation of the aorta centerline. The thrombus contour is modeled as a function of the radial distance to the computed centerline. The volume of interest is resampled into polar coordinates centered in the aorta centerline.

The thrombus content is further segmented into thrombus connected components (TCC) (Section 3.2). Using this polar coordinate reference system, the watershed segmentation obtains the TCCs in the thrombus region at both radial and slice level using heuristics based on *a priori* knowledge and spatial

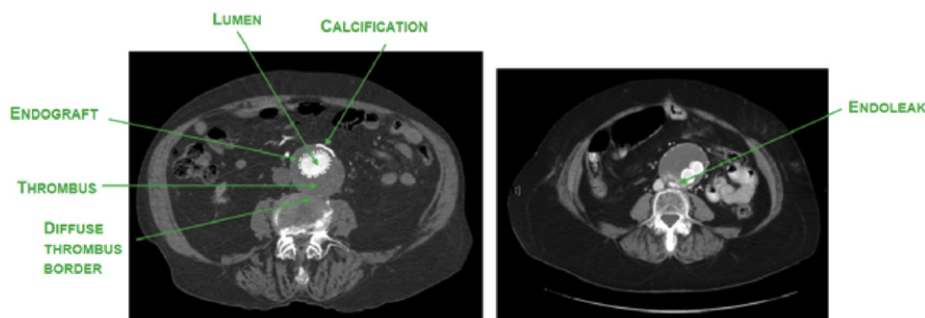


Fig. 1. Slice showing abdominal aortic aneurysm with different parts (left). A type II endoleak appears as bright tissue in the thrombus area.

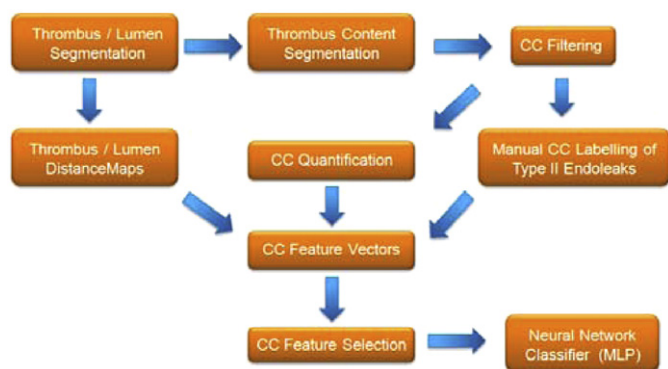


Fig. 2. Processes of the automatic endoleak classification system.

coherence. The radial distance functions that describe the thrombus contour are obtained from the resulting connected components and define the target segmented region. The main advantages of this method are its robustness and speed, compared with the state of the art approaches described above. It does not employ sophisticated numerical methods nor needs fine parameter tuning. The TCC features are extracted to be used for classification (Section 3.3). Once all the features for the TCCs are obtained, these are manually labelled by the experts as endoleaks or not endoleaks. A feature selection is performed (Section 3.4) to remove redundant or confusing features. This data is used as input for the training and validation of the MLP neural network classifier. Our approach to endoleak detection is based on *a priori* knowledge of the possible location and appearance of endoleaks in CTA images according to what it is described in medical papers, the indications given by expert interventional radiologists, and their manual labelling of relevant TCCs corresponding to endoleaks.

### 3.1. Lumen and thrombus segmentation

A robust segmentation of the lumen and thrombus of the AAA is required as an input for the automatic endoleak detection system, in order to isolate the lumen and thrombus area. As seen in the right hand of Fig. 1, thrombus may be touching with other structures of similar intensity, so their boundaries are quite difficult to find, even for a trained radiologist. In this section, we describe the lumen segmentation, centerline extraction and thrombus segmentation. Our thrombus segmentation approach is based on a radial description of the thrombus contours.

#### 3.1.1. Region growing-based lumen segmentation

Segmentation of the lumen is based on a 3D region growing algorithm [8] computed on the CTA volume. First, a volume of interest (VOI) is defined in order to reduce the extent of the data and then preprocessed to reduce noise. A manually given seed point on the lumen is at least required for the region growing algorithm. The algorithm includes voxels whose intensity values lie in a confidence interval defined over the current segmented region over an iterative process. At each iteration, all neighborhood voxels are visited and the confidence criterion is evaluated. Then, statistics are recomputed and the next iteration begins. The resulting identified region is smoothed by morphological closing, to fill possible small holes.

#### 3.1.2. Centerline extraction

The centerline computed as the approximate centroid of the lumen region at each slice is a good approximation of the morphological skeleton of the whole aorta. It serves as the

starting point for the thrombus segmentation. A single point on the centerline is obtained for every slice using 2D image moments, since the aorta is almost normal to axial slices. Image moments provide information on the spatial distribution of a given image region corresponding to a structure. The moments of a 2D image are defined as

$$M_{p,q} = \sum_{y=0}^{Y-1} \sum_{x=0}^{X-1} x^p y^q I(x,y), \quad (1)$$

where  $I(x,y)$  is a discrete image. The centroid is defined as the pair  $[M_{10}/M_{00}, M_{01}/M_{00}]$ .

At each slice, we select the 2D connected components obtained from the 3D lumen region corresponding. We compute the centroid of each such 2D lumen connected components. The centroid which is the nearest to the centerline point detected in the previous slice is kept as the next centerline point. Algorithm 1 yields a series of points that conform the centerline of the segmented lumen.

**Algorithm 1.** Centerline extraction from 3D lumen region.

- 1: Initialization of region: center line in first processed slice
- 2: **for** all slices in 3D image **do**
- 3: Identify lumen connected components from the 3D lumen region
- 4: **for** each lumen component in slice **do**
- 5: Compute centroid
- 6: Compute Euclidean distance to centerline point in previous slice
- 7: **end for**
- 8: Keep nearest centroid as the centerline point
- 9: **end for**

#### 3.1.3. Thrombus segmentation

We model the internal and external radius of the thrombus of the aneurysm as radial distance functions in cylindrical coordinates. We can express the volume of interest around the lumen centerline as

$$\Psi = \Psi(r, \theta, z). \quad (2)$$

At every  $z$  value, corresponding to a slice of the CTA volume, we choose the origin of these functions to be the centerline point at the corresponding slice. The external and internal radii of the thrombus and the aneurysm can be defined as two contours given by functions of the angle in polar coordinates:

$$\begin{aligned} T_{rint} &= \Psi_{rint}(\theta, z), \\ T_{rext} &= \Psi_{rext}(\theta, z). \end{aligned} \quad (3)$$

This idea is depicted in Fig. 3. The segmentation procedure consists of calculating the values of the internal and external radii  $T_{rint}$  and  $T_{rext}$  at every angle, which define the closed boundaries enclosing the region corresponding to the thrombus.

Conversion from Cartesian to polar coordinates requires resampling the input VOI. For every slice, a new image is obtained, where the  $X$  coordinate represents the radius, starting from the centerline point at the left, and the  $Y$  coordinate represents the angle  $\theta$ , covering  $360^\circ$  with the origin at the top. This polar representation is visualized as an image in Fig. 4(b). The original CTA slice is shown in 4(a).

The polar representation presents several advantages. First, the VOI is converted to a quasi cylindrical VOI (it is not exactly cylindrical, because the centerline is not a vertical line), instead of the typical rectangular prism, but after that it is treated as a standard volume with a regular grid. Second, computation speed

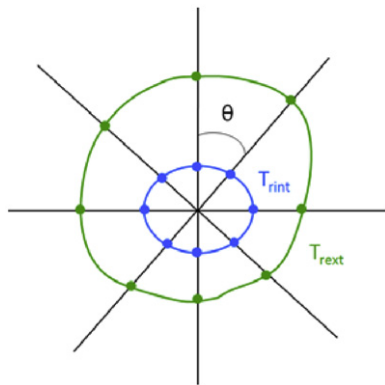


Fig. 3. Radial model for the thrombus segmentation.

is increased, since resampling is only performed once and the polar slices are processed as conventional 2D images.

Next, polar slices are filtered using a median filter to remove speckle and additive noise coming both for the original image and the image resampling needed for the polar transformation visualization. In order to remove the lumen and the stent from the images without affecting the thrombus voxels, every slice is thresholded in such a way that those image values higher than a threshold  $Th_{lmm}$  are converted to a value  $I_{bgr}$ , which approximates the background value of the tissue around the thrombus. In our experiments we chose  $Th_{lmm}=150$  HU<sup>1</sup> and  $I_{bgr}=-100$  HU. The result of these operation is shown in 4(c). After noise filtering and lumen/stent thresholding, the thrombus appears as the brightest structure closest to the centerline and we can use this *a priori* information for the segmentation.

The internal thrombus radius  $T_{rint}$ , which corresponds to the lumen external contour when no endoprosthesis is present, can be found moving away from the centerline (which corresponds to moving along a row in the polar slice image), as the boundary where values different from  $I_{bgr}$  appear. The median filter removes the small regions with lower image values that may exist in between.

Localization of the external radius of the thrombus on each slice in polar coordinates is achieved by a local analysis based on two concepts: *radial connected components* (RCC) and *slice connected components* (SCC). We define an RCC as a connected segment over a row of a polar slice and an SCC as a 2D connected component on a polar slice. First, a row-by-row analysis is performed in all slices to create an image of RCCs of each slice. An RCC is created for consecutive pixels of a row that follow a given membership criterion. We use the absolute difference from the mean of the currently detected RCC with a threshold value  $Th_{RCC}$  (we use  $Th_{RCC}=20$  HU in our experiments). Obtaining  $T_{rint}$  and RCC at each row can be done simultaneously. The algorithm 2 illustrates the process for creating the RCCs:

**Algorithm 2.** Creating the Radial Connected Components (RCC).

- 1: Move to the origin of the first polar slice (upper left corner)
- 2: **for** all polar slices **do**
- 3:   **for** all rows in the current polar slice **do**
- 4:     create a new RCC and insert first pixel on the current row
- 5:     **for** all pixels in the current row **do**
- 6:       **if** (intensity(pixel)  $\in$  intensity confidence interval of the currentRCC) **then**

- 7:       insert pixel in the current RCC
- 8:     **else**
- 9:       calculate and store row internal thrombus radius
- 10:    **end for**
- 11:   **end for**
- 12: **end for**

Next, we proceed to filter the RCCs. First, RCCs whose average values are not in the intensity range of  $Th_{low}-Th_{high}$  are removed. In our experiments we used  $Th_{low}=0$  HU and  $Th_{high}=200$  HU which are conservative values to characterize the thrombus image intensity, which apply to most AAA CTA datasets. Second, RCCs that do not start from a distance  $d_{max}$  from the external lumen radius are removed too. This criterium is based on the fact that, if a thrombus exists, this must be almost close to the previously thresholded area for lumen and endoprosthesis. In our experiments we also chose  $d_{max}=5$  mm. Also in a very conservative manner. Results of the RCC computation procedure are shown in Fig. 5. It can be seen that the thrombus has been almost completely isolated, but some RCCs that are not part of the thrombus still remain (see Fig. 5(b)).

SCCs are computed using 2D connectivity and the same intensity criteria used for the RCCs. Each SCC keeps a list of RCCs which are included in it. SCCs are used to filter RCCs by using spatial coherency information on each slice. First, SCCs (and corresponding RCCs) that contain less than  $N_{min}$  voxels (we use  $N_{min}=10$ ) are discarded since they are not significant at a slice level. Next, SCCs are filtered by the position of the centroid, having into account that most of the candidate RCCs at this moment are part of the thrombus. For each slice, the position of the centroid for all the RCCs and the corresponding centroid median value are calculated. The median value is a good indicator for the real position of the thrombus. Then we compute the distance from the centroid of every SCC on that slice to the median centroid value, and if the distance is greater than a threshold  $d_{centroid}=20$  mm, the SCC is completely removed.

Initial values for the thrombus contours  $T_{rint}$  and  $T_{rext}$  are obtained by taking, for every row on all slices, the first index of the first RCC and the last index of the last RCC on that row (it is assumed that the RCCs remaining after filtering are part of the thrombus). This results in a good approximation to the real external thrombus contour, with the exception of some areas where the thrombus region invades adjacent structures and that represent a discontinuity in  $T_{rext}$  (see Fig. 6 blue contours). In order to solve this problem and regularize the contours, a continuity constraint is imposed over  $T_{rext}$  and the contour points whose radii are part of a discontinuity are interpolated. Discontinuities are identified as significant radius changes from line to line in the polar image. Then, the radii in these areas are linearly interpolated in order to obtain the final result (green contours in Fig. 6).

### 3.2. Thrombus connected component extraction

After the initial thrombus and lumen segmentation, the thrombus is further segmented in thrombus connected components (TCCs) which will be later classified as being endoleaks or not. This segmentation is based on a topological grayscale watershed transform [3] applied on a slice by slice basis in the area of the segmented thrombus on each slice (see Fig. 7). First, the image is smoothed using an edge-preserving smoothing filter based on a level-set modified curvature diffusion equation (MCDE) [17]. Two parameters are required for the filter: the conductance parameter, which controls the strength of the edges to preserve and the number of smoothing iterations, which controls the degree of smoothing. After filtering, in order to define the watersheds basins, we then calculate the image gradient magnitude.

<sup>1</sup> HU=Hounsfield Units, a normalized CT image intensity value representing X-ray absorption.

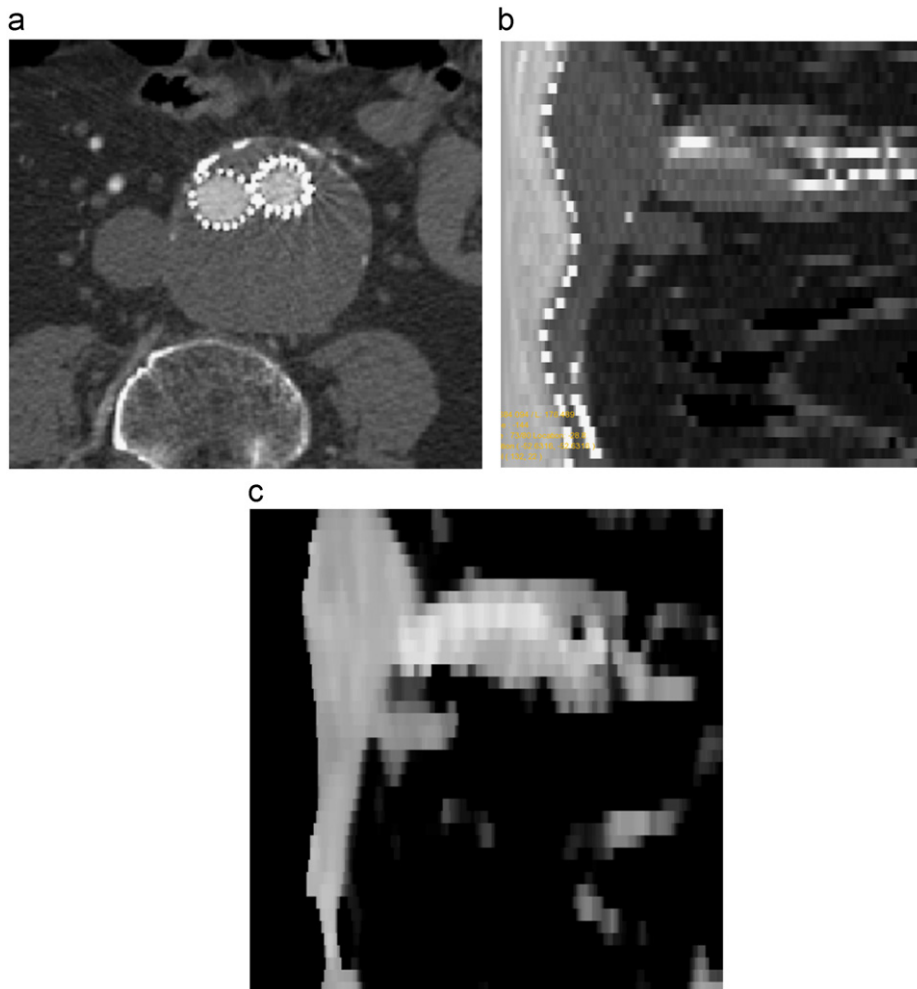


**Fig. 4.** (a) AAA after EVAR viewed on axial slice, (b) polar representation, and (c) median filtered version with lumen and stent thresholded and removed. The origin for the polar coordinate representation of (b) is taken as the centerline in (a).

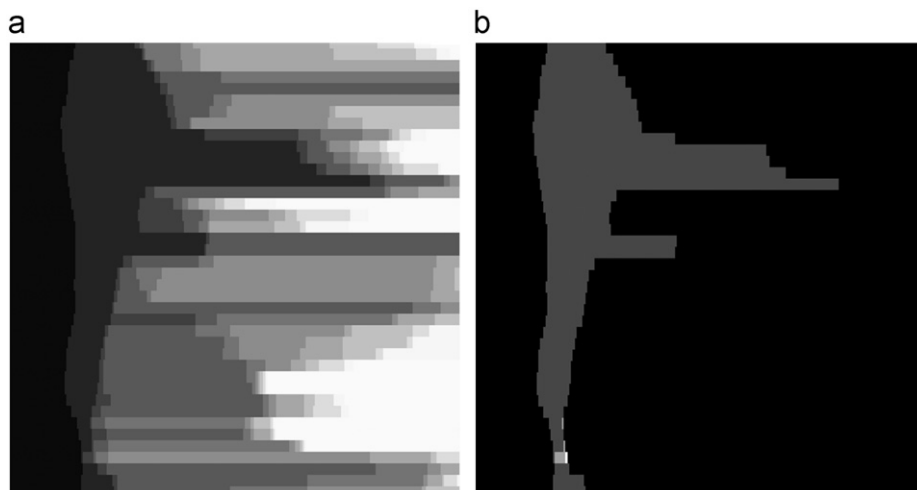


**Fig. 5.** (a) RCCs computed from Fig. 4(c). Different RCCs found along each row are represented in different colors (from darker to brighter). (b) Filtered RCCs.

The topological grayscale watershed transform is an algorithm for calculating the well-known watershed transform [1] in which the image is segmented based on its topology. The gradient magnitude is interpreted as an elevation map and the image relief is flooded dividing it into catchment basins. The pixels of each basin share a local minima and the basin boundaries

corresponds to the image edges. The watershed transform calculation is controlled by a single parameter, the water level, that controls the height of the flooding, merging adjacent regions as the ‘water’ ascends to reduce the effect of oversegmentation.

The parameters for all filters involved in this segmentation are chosen in order to distinguish the endoleaks from the background

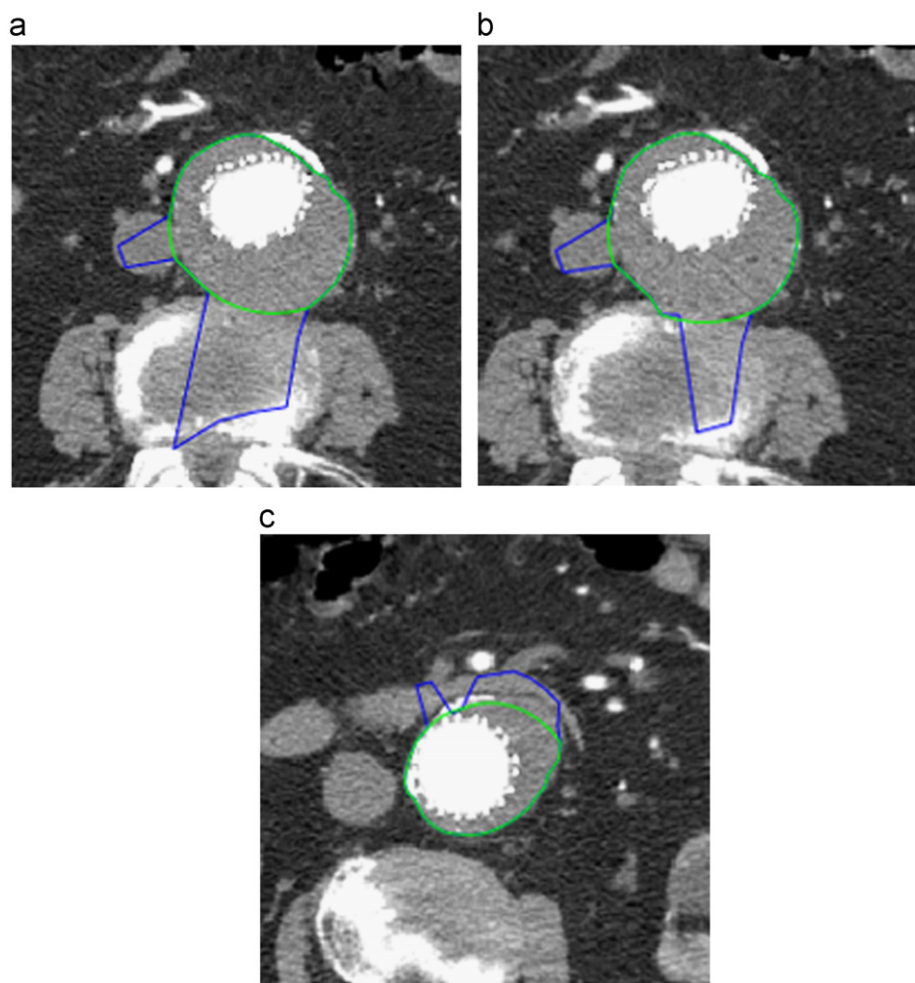


**Fig. 6.** Thrombus segmentation results. Correction (green line) of the initial external thrombus radius (blue line). Examples of appropriate correction (a) and (b) and underestimation (c). (For interpretation of the references to color in this figure legend, the reader is referred to the web version of this article.)

region corresponding to the thrombus, or other adjacent structures. Endoleaks can correspond to a single or several TCCs (oversegmentation) if the water level is low. If it is high, we would have TCC corresponding to both endoleak and other tissues (undersegmentation). Classifying oversegmented endoleaks is not a problem, but solving the undersegmentation problem is not easy, therefore the water level parameter is set to avoid undersegmentation.

### 3.3. Feature extraction from TCC

We calculated the following geometric features for each labelled TCC that will be used by the MLP-based classification system to determine if the TCC is part of an endoleak region:

- **Area:** number of pixels of the TCC.
- **Area-region Ratio:** ratio of the TCC's bounding box and the area.
- **Binary Principal Moments:** TCC's principal moments of inertia (two features).
- **Equivalent Radius:** radius of a circle of the same area as the TCC and the following image content-based statistical features computed from the image intensity of the CTA image region corresponding to the TCC: *Mean*, *Sigma*, *Median*, *Kurtosis*, *Skewness* and *Elongation* (ratio of the largest to smallest principal image moments).

Besides these features, we need to incorporate another feature that describes the relative position of the TCC with respect to the lumen and thrombus boundaries. We can profit from the observation that type II endoleaks typically appear close to the thrombus boundary and perfusing inwards. We need this feature to be normalized, since the radius and shape of the thrombus and lumen, and the eccentricity of the lumen with respect to the thrombus is not uniform. Moreover, the lumen can show two branches when the aorta splits into two forming the iliac arteries (see Fig. 7(a)), so we cannot take the distance to the lumen centroid. Taking all this considerations into account, we propose a feature called normalized thrombus distance (NTD). Two distance maps are first calculated from the thrombus boundary inwards ( $\delta_{lm}$ ), and from the lumen thrombus boundary outwards ( $\delta_{th}$ ), using Danielsson's algorithm [4] (see distance visualization in Fig. 8). In the rest of image regions the NTD value is zero. Then, we calculate the NTD as:

$$NTD = \begin{cases} \frac{\delta_{lm}}{\delta_{th}} & \text{if } \delta_{lm} \leq \delta_{th}, \\ \frac{\delta_{th}}{\delta_{lm}} & \text{if } \delta_{th} \leq \delta_{lm}. \end{cases} \quad (4)$$

The NTD takes its maximum value of one at thrombus points that are equidistant to the lumen and thrombus boundaries. NTD minimum value is zero and it is taken at the thrombus boundary

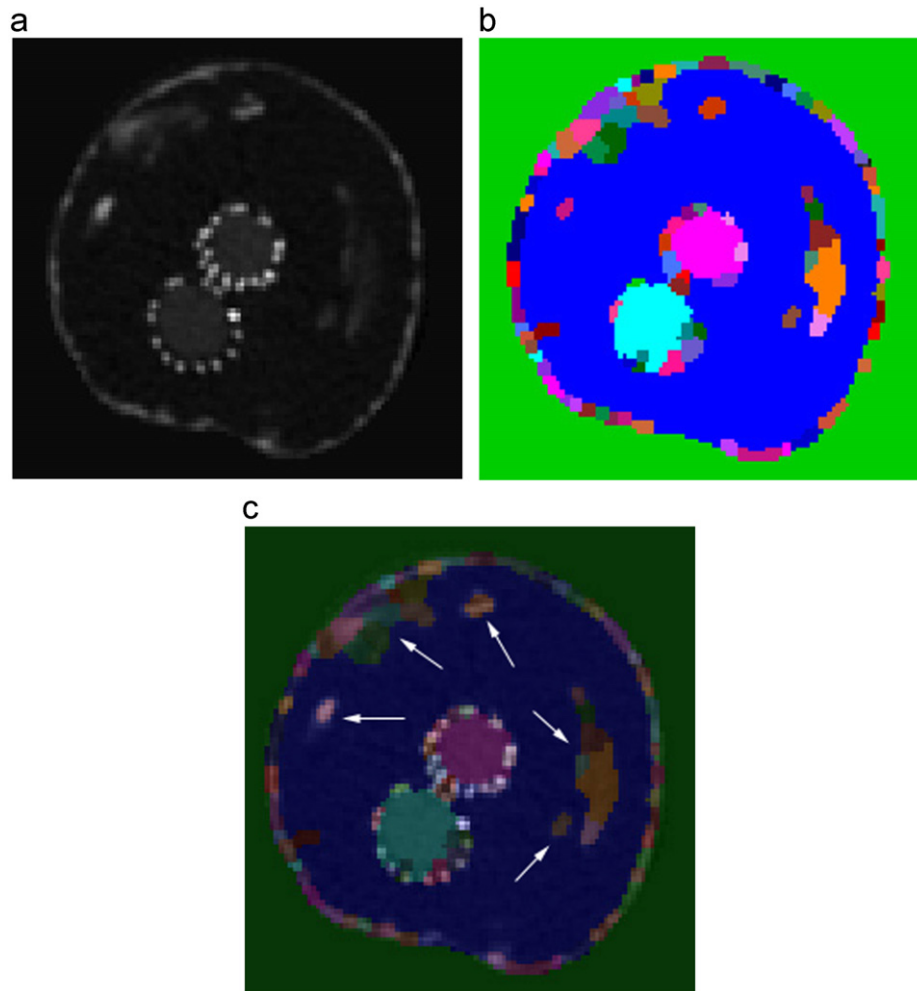


**Fig. 7.** Extraction of Thrombus CCs. (a) Source slice with visible endoleaks, (b) result of Watersheds segmentation, and (c) blended result. Endoleaks are indicated by arrows in (c). Each endoleak corresponds to more than one coloured region (oversegmentation).

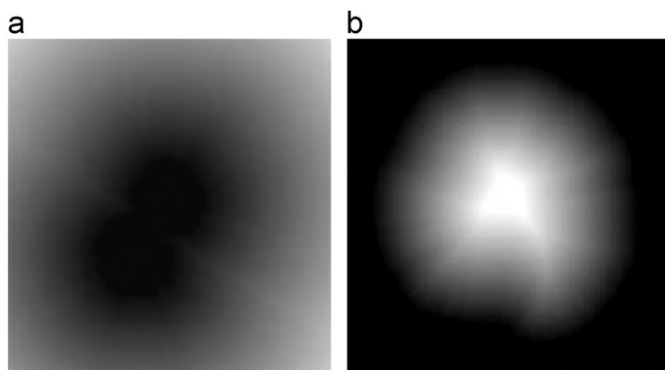


**Fig. 8.** Visualization of the distance maps used to calculate the NTD feature. (a) Distance to the lumen  $\delta_{lm}$  and (b) distance to the thrombus  $\delta_{th}$ .

and outside the thrombus, and at the lumen boundary and inside the lumen. NTD takes values in  $[0,1]$  inside the thrombus. For the thrombus and lumen boundaries used as input for the NTD, we can use the segmentation described in 3.1 or a manual segmentation.

### 3.4. Reduced feature vector for MLP

Let us call the dependent indicative variable *IsLeak*. Its value is 0 for negative TCC and 1 for TCC inside endoleaks. In order to reduce the classifier system's complexity and increase the speed

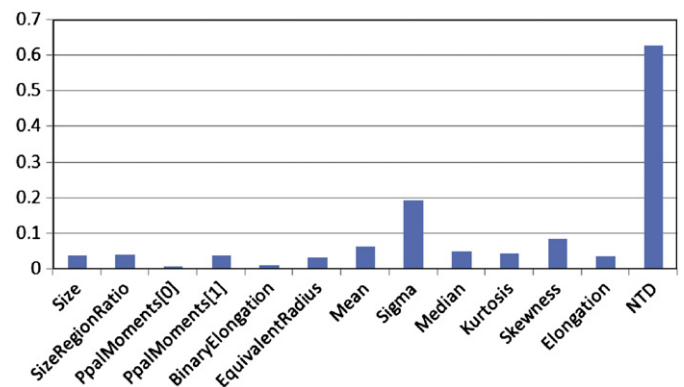


**Fig. 9.** Absolute value of Pearson correlation coefficients of each feature with the indicative variable *IsLeak*.

of the calculations, a subset of features is selected as input for the network based on the absolute value of the Pearson correlation coefficients between the dependent variable *IsLeak* and the rest of variables (features) defined as:

$$r = \frac{\sigma_{XY}}{\sigma_X \sigma_Y} \quad (5)$$

In Fig. 9 we can see the results of calculating the absolute value of the Pearson Coefficients for the CCs of all the slices in the

aneurysm region for a given dataset. As expected, we can see that the NTD feature is highly correlated with the dependent variable, since the feature was designed to incorporate the *a priori* knowledge of the spatial distribution of the endoleaks. We can see that the standard deviation value is also important, meaning that the image intensity value, also as expected, should play an important role in the characterization of endoleaks. The experimental results show that the reduced feature vector obtained by this straightforward approach give comparable classification results.

#### 4. Experimental data and results

Our radial-based thrombus segmentation method has been tested on real human CTA datasets featuring endoleaks confirmed by radiologists, obtained from a LightSpeed16 CT scanner (GE Medical Systems, Fairfield, CT, USA) with  $512 \times 512 \times 354$  voxel resolution and  $0.725 \times 0.725 \times 0.8$  mm spatial resolution. Two points inside the lumen, defining the limits of the thrombus region in axial direction, were manually selected as seed points for the 3D region growing segmentation of the lumen. The lumen centerline is then extracted from it to be used as the origin for the polar representation in an area of radius 10 mm around the centerline at each slice. Finally, the described radial function-based model is used to segment the thrombus. Finally, the described radial function-based model is used to segment the thrombus. Some examples of results of the thrombus segmentation method have been shown in Fig. 6 where the initial estimation (blue) and the corrected external thrombus contours (green) are shown.

The classification scheme was tested independently on each single CTA volume from patients with type II endoleak after EVAR treatment. The whole volumes consisted of 383 slices in a  $512 \times 512$  matrix, with an in-plane spatial resolution of 0.703 mm and a slice thickness of 0.8 mm. Due to the scarce availability of volumes from patients affected with endoleaks, we tested our approach independently on each volume, working on a 2D slice-by-slice basis.

In each case, we took as input for the MLP training the results of a segmentation of the lumen and thrombus regions validated by expert radiologists. The watershed-based segmentation was performed on the slices corresponding to the aneurysm region in each dataset using the implementation provided by the *Insight Toolkit* [8] for the topological grayscale watershed transform. We used the following parameters for the different filters involved in the watershed segmentation: smoothing conductance=50.0, smoothing number of iterations=10, watersheds water level<sup>2</sup>=9.0. The NTD distance-map feature was calculated from the input thrombus and lumen segmentations. The TCCs were manually labelled as being part of an endoleak. From the group of negative TCCs, we proceeded to select randomly an equal number of samples in order to obtain a balanced training/testing set.

Classification experiments were performed using the MLP implementation provided in [20]. The MLP neural network consisted feature described in Section 3.3, a hidden layer with three neurons and two binary outputs, with sigmoid functions. Network training and validation were performed using 10-fold cross-validation in all computational experiments. Initially, we used the full training/test set consisting of the full feature vectors described in Section 3.3. The results are shown in Table 1. Results are above 90% accuracy, with a high sensitivity which is very interesting because the cost of false negatives is much higher than that of false positives.

**Table 1**

Classification results for the training/test data build from full feature vectors, 10-fold crossvalidation. The table shows the total accuracy, sensitivity and specificity for each dataset. Last row shows the average across datasets. All calculations were performed with three hidden nodes, learning rate=0.3 and training time=550 epochs.

Dataset	Accuracy	Sensitivity	Specificity
1	92.39	93.43	91.36
2	93.68	93.66	93.69
3	93.09	93.66	92.52
4	93.21	94.13	92.29
5	92.16	93.43	90.89
Av.	92.90	93.66	92.15

**Table 2**

Classification results for the training/test data build from reduced feature vector, 10-fold crossvalidation. The table shows the total accuracy, sensitivity and specificity for each dataset. Last row shows the average across datasets. All calculations were performed with 3 hidden nodes, learning rate=0.3 and training time=550 epochs.

Dataset	Accuracy	Sensitivity	Specificity
1	93.79	94.84	92.76
2	94.73	94.37	95.09
3	93.68	94.60	92.76
4	93.33	94.13	92.52
5	92.74	93.90	91.59
Av.	93.65	94.37	92.94

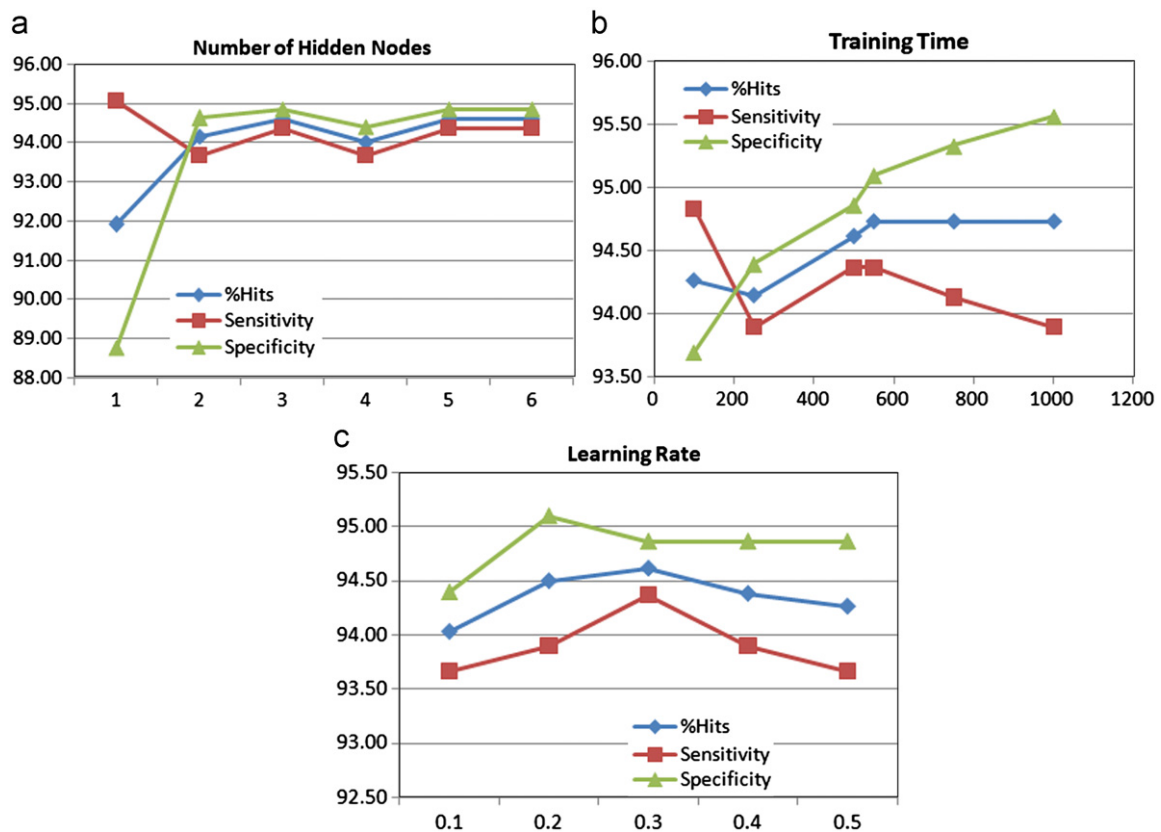
Next, we test the improvement in the classification results by testing reduced sets of features selected according to the correlation results found in Section 3.4 (Fig. 9). The best results were obtained by selecting the following features: *Area*, *Mean*, *Sigma* and *NTD*. We can see in Table 2 that the classification rate improves, reaching 93.65% accuracy with a sensitivity of 94.37% and a specificity of 92.94%. The best results give a success rate of 94.73% with a sensitivity of 94.37% and a specificity of 95.09% for the second dataset.

Fig. 10 shows the influence of several parameters of the MLP in the classification performance measures. We can see that the best results are obtained for a training time of 550 epochs, a learning rate=0.3 and 3 hidden nodes. These sensitivity experiments were performed on the training/test dataset that gives best results on the reduced feature vector (dataset 2).

#### 4.1. Discussion, conclusions and future work

As can be seen in Fig. 6, the method developed for thrombus segmentation shows good results in defining the external contour, where thrombus density is very similar to that of adjacent structures, and very prone to segmentation error in areas close to them. The obtained contour is very accurate due to the assumption of a radial model. The method needs the settings of several thresholds to work. However, our experience demonstrates that the sensibility of the method to these parameters is low as they were chosen very conservatively. A deeper sensibility analysis is beyond the scope of this paper. One of the main advantages of the method is its computational speed. It took less than 20 s to process 80 slices on a Pentium Core 2 Quad at 2.4 GHz. However, the method requires further improvements, since we have observed an underestimation of the radius in some places which were identified as leaks (see Fig. 6(c)). Results of this segmentation are comparable to the state of the art found in the literature [10] with less human

<sup>2</sup> As a percentage of current image dynamic intensity range.



**Fig. 10.** Influence of neural network parameters. Accuracy, sensitivity and specificity are calculated. Parameters tested are number of hidden nodes (a), learning rate (b) and training time measured in number of epochs (c).

intervention. Our algorithm does not depend on any user-defined contour or initial manual segmentation. User interaction is minimal: it only needs two seed points contained in the lumen and defining the range of slices of interest. Accurate segmentations are obtained in areas where it is difficult to distinguish the thrombus from adjacent structures. Moreover, the speed of the whole process makes it also suitable for routine clinical use.

We have also demonstrated an automatic system for the detection of (Type II) endoleaks in CTA images of abdominal aortic aneurysms. The classification results show that the system is able to detect endoleaks with high accuracy based on the analysis of extracted TCCs. The use of neural networks is specially adequate for this case, since we do not need to explicitly incorporate the clinical *a priori* knowledge in terms of precise parameters and thresholds for image intensities, distances, etc. This is a common characteristic in many classification problems in medical imaging, in which the specialist is able to discriminate at first sight the object of interest, but is not able to explicitly indicate the rules that guide their mental discourse while diagnosing, which is usually the product of accumulated experience and observations.

Classification results over several real datasets shown in Tables 1 and 2 show that the system obtains accuracy results above 90% with high sensitivity, which is specially important given the high cost of not recognizing endoleaks present in the image. We have also demonstrated that a careful selection of features decreases the complexity of the problem and improves the results. There is no similar work in the literature, therefore the results can be assumed as a initial reference for future works.

Regarding the parameters used for the MLP model, in the case of using five features, we have seen that results are very similar when the number of hidden units is two or more. Using five, six or

more nodes does not improve the results and so the best balance is found with three nodes. It can be seen that the influence of the learning rate is limited when the number of epochs is high enough (around 500). With respect to the training time, best results are obtained with 550 epochs and global classification results do not improve by increasing this number. However, the plots show that the sensitivity decreases as the specificity increases, keeping a constant rate of total hits. This is undesirable since we want the sensitivity to be high, and thus the optimum is found at 550 epochs.

Future work to improve the thrombus segmentation algorithm will be oriented to improve the thrombus model, fine-tune the parameters of the process for a large number of datasets and validate the segmentation by comparison with manual segmentations and other methods. In the near future, we expect to extend the system to 3D analysis of TCCs, and to the detection of endoleaks obtained from several datasets. Since the diagnosis of endoleaks is not totally certain, we also expect to incorporate a fuzzy or probabilistic description in order to determine which TCCs are endoleaks. Another possible improvement to the system, is the classification of other types of endoleaks (I, III, IV and V), since currently the system was trained only to identify type II endoleaks. This would probably need the incorporation of other types of features for the analysis. Finally, the system would need deeper clinical validation in order to integrate it in clinical environments for diagnosis support of the evolution of AAAs treated with EVAR.

**Conflict of interest statement**

None declared.

## References

- [1] S. Beucher, Ch. Lantuejoul, Use of watersheds in contour detection, in: International Workshop on Image Processing, Real-Time Edge and Motion Detection/Estimation, 1979.
- [2] A. Borghi, N.B. Wood, R.H. Mohiaddin, X.Y. Xu, 3D geometric reconstruction of thoracic aortic aneurysms, *BioMedical Engineering OnLine* 5 (59) (2006).
- [3] M. Couprie, G. Bertrand, Topological grayscale watershed transform, *SPIE Vision Geometry VI*, vol. 3168, 1997, pp. 136–146.
- [4] P.E. Danielsson, Euclidean distance mapping, *Computer Graphics and Image Processing* 14 (1980) 227–248.
- [5] M. de Bruijne, B. van Ginneken, M.A. Viergever, W.J. Niessen, Interactive segmentation of abdominal aortic aneurysms in CTA images, *Medical Image Analysis* 8 (2) (2004) 127–138.
- [6] G.S.K. Fung, S.K. Lam, S.W.K. Cheng, K.W. Chow, On stent-graft models in thoracic aortic endovascular repair: a computational investigation of the hemodynamic factors, *Computers in Biology and Medicine* 38 (4) (2008) 484–489.
- [7] J.A. Hertz, A.S. Krogh, R.G. Palmer, Introduction To The Theory Of Neural Computation, Volume I (Santa Fe Institute Studies in the Sciences of Complexity), Westview Press, 1991.
- [8] L. Ng, J. Cates, L. Ibanez, W. Schroeder, The ITK Software Guide, Kitware Inc., 2003.
- [9] R.J.F. Laheij, J. Buth, P.L. Harris, F.L. Moll, W.J. Stelter, E.L.G. Verhoeven, Need for secondary interventions after endovascular repair of abdominal aortic aneurysm. Intermediate-term follow-up results of a european collaborative registry, *British Journal of Surgery* 87 (12) (2002) 1666–1673.
- [10] K. Lee, R.K. Johnson, Y. Yin, A. Wahle, M.E. Olszewski, T.D. Scholz, M. Sonka, Three-dimensional thrombus segmentation in abdominal aortic aneurysms using graph search based on a triangular mesh, *Computers in Biology and Medicine* 40 (3) (2010) 271–278.
- [11] S.D. Olabarriaga, J.M. Rouet, M. Fradkin, M. Breeuwer, W.J. Niessen, Segmentation of thrombus in abdominal aortic aneurysms from CTA with nonparametric statistical grey level appearance modelling, *IEEE Transactions on Medical Imaging* 24 (4) (2005) 477–485.
- [12] S.W. Stravopoulos, S.R. Charagundla, Imaging techniques for detection and management of endoleaks after endovascular aortic aneurysm repair, *Radiology* 243 (3) (2007) 641–655.
- [13] M. Subasic, S. Loncaric, E. Sorantin, 3d image analysis of abdominal aortic aneurysm, in: M. Sonka, M. Fitzpatrick (Eds.), *SPIE Medical Imaging*, vol. 4684, 2002, pp. 1681–1689.
- [14] A.J. Tolia, R. Landis, P. Lamparello, R. Rosen, M. Macari, Type II endoleaks after endovascular repair of abdominal aortic aneurysms: natural history, *Radiology* 235 (May) (2005) 683–686.
- [15] G.R. Upchurch, T. A. Schaub, Abdominal aortic aneurysm, *American Family Physician* 73 (7) (2006) 1198–1204.
- [16] J.J. Wever, J.D. Blankensteijn, J.C. Van Rijn, I.A. Broeders, B.C. Eikelboom, W.P. Mali, Inter- and intraobserver variability of ct measurements obtained after endovascular repair, *American Journal of Roentgenology* 175 (2000) 1279–1282.
- [17] R.T. Whitaker, X. Xue, Variable-conductance, level-set curvature for image denoising, *International Conference on Image Processing (ICIP'01)*, vol. 3, 2001, pp. 142–145.
- [18] G.H. White, J. May, R.C. Waugh, Type I and type II endoleak: a more useful classification for reporting results of endoluminal aaa repair, *Journal of Endovascular Surgery* 5 (4) (1998) 378–380.
- [19] G.H. White, J. May, R.C. Waugh, X. Chaufour, W. Yu, Type III and type IV endoleak: toward a complete definition of blood flow in the sac after endoluminal aaa repair, *Journal of Endovascular Surgery* 5 (4) (1998) 305–309.
- [20] I.H. Witten, E. Frank, L. Trigg, M. Hall, G. Holmes, S.J. Cunningham, Weka: practical machine learning tools and techniques with java implementations, in: K. Ko, N. Kasabov (Eds.), *ICONIP/ANZIIS/ANNES'99 Workshop on Emerging Knowledge Engineering and Connectionist-Based Information Systems*, Dunedin, New Zealand, 1999, pp. 192–196.
- [21] F. Zhuge, G.D. Rubin, S. Sun, S. Napel, An abdominal aortic aneurysm segmentation method: level-set with region and statistical information, *Medical Physics* 33 (5) (2006) 1440–1453.